Supplemental Material: Signatures of a quantum Griffiths phase close to an electronic nematic quantum phase transition

Pascal Reiss,[1,*] David Graf,[2] Amir A. Haghighirad,[1,3] Thomas Vojta,[4] and Amalia I. Coldea[1,†]

[1] *Clarendon Laboratory, Department of Physics, University of Oxford, Oxford, UK*
[2] *National High Magnetic Field Laboratory, Florida State University, Tallahassee, FL, USA*
[3] *Institute for Quantum Materials and Technologies,*
Karlsruhe Institute of Technology, Karlsruhe, Germany
[4] *Department of Physics, Missouri University of Science and Technology, Rolla, MO, USA*

(Dated: October 6, 2021)

This Supplemental Material contains additional data and analysis which enhance the findings presented in the main paper.

Sample variation and pressure dependence

The samples A-C reported in the main manuscript were discussed in a previous study dedicated to quantum oscillations [1]. We mapped out the suppression of the nematic phase in $\mathrm{FeSe}_{0.89}\mathrm{S}_{0.11}$ for sample A under pressure and identified a critical pressure $p_c = 5.8$ kbar at which the nematic phase is suppressed [1]. Sample A was measured inside a piston cylinder pressure cell in fields up to 13.5T, and the pressure was determined from the superconducting transition of Sn at low temperatures.

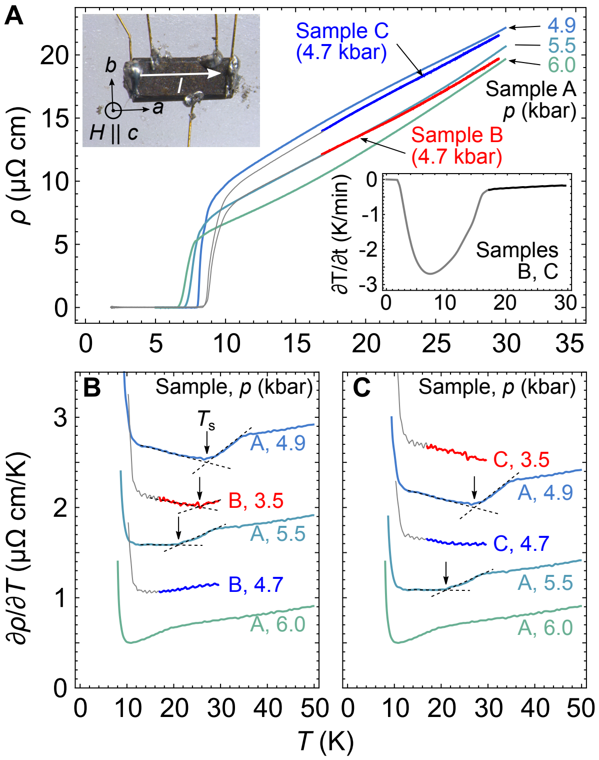

FIG. SM1. (**A**) Temperature dependence of the zero-field resistivity under pressure for samples A, B and C. The lower inset shows a faster cooling rate for samples B and C below 17 K restricting the temperature interval for comparing sample resistivities. Resistivities of samples B and C below 17 K are shown as gray lines. The top inset shows a photograph of sample A, with the tetragonal unit axes a and b and the current direction I indicated. The magnetic field was applied along $H||c$. (**B,C**) First derivative of the zero-field resistivities shown in panel A from which the structural transition temperature T_s can be extracted.

In this Letter, we focus on the magnetotransport behavior of samples B and C, which were measured simultaneously in a piston cylinder pressure cell in a hybrid magnet with field sweeps between 11.4-45 T. Here, the applied pressure was determined by means of the Ruby florescence method below 4 K.

Even though all samples originate from the same batch, it is important to note that very small variations in sulfur content are expected to occur between different crystals. This is mainly due to the thermal gradient generated during the chemical vapor growth [2] and hence

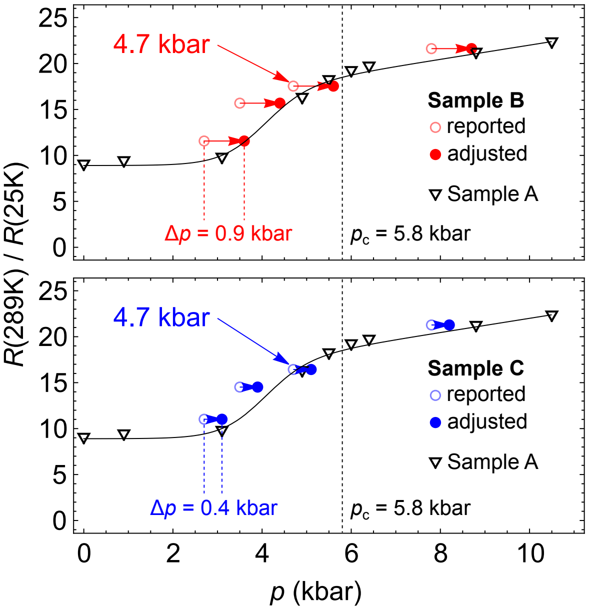

FIG. SM2. Pressure evolution of the residual resistivity ratio (RRR) of samples A, B and C. This ratio, which is a contact-layout independent measure, can be used to estimate the pressure offset for samples B (top) and C (bottom), as indicated by the horizontal arrows.

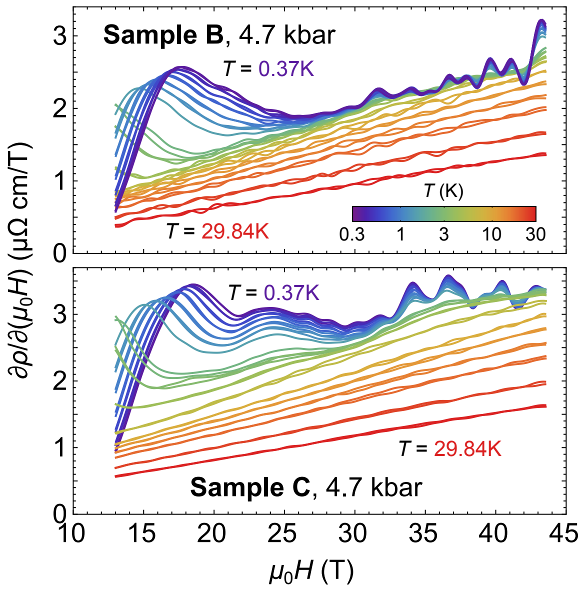

FIG. SM3. First derivatives of the magnetoresistivity for samples B (top) and C (bottom) at different low temperatures up to 45 T. Note the presence of a strong low-frequency quantum oscillation visible in sample C at low temperatures, but absent in sample B.

a locally varying growth temperature along the ampule which leads to locally varying gas pressures. In order to minimize the sample variation, we screened more than 20 samples in zero field at ambient pressure. We chose to study in detail the cleanest samples with the largest residual-resistivity ratio from transport measurements with a similar nematic transition temperature. All single crystals used naturally grew as platelets with well defined facets along the tetragonal unit axes, with the crystallographic c axis perpendicular. The inset to Figure SM1A shows a photograph of sample A. Electrical contacts were attached such that the current was applied along the tetragonal a axis. For all studies, the magnetic field was applied along the c axis. Note that in the nematic phase, the unit cell rotates by 45° along c.

In order to compare all samples, and to estimate their proximity to the nematic quantum phase transition, we use the pressure scale established for sample A, where the nematic quantum phase transition occurs for 5.8 kbar [1]. A “pressure correction” is applied for samples B and C based on their low-temperature resistivity dependencies, in order to account for varying sulfur contents. We note that the nematic phase is suppressed both with pressure and with increasing sulfur content and hence we expect that a higher sulfur content leads to a reduction of the critical pressure. Fig. SM1A show the resistivity versus temperature for all samples A-C. Evidently, the low-temperature resistivity is suppressed with increasing pressure, as shown for sample A. The resistivity of Sample B at 4.7 kbar traces almost exactly the cooling curve of sample A at 5.5 kbar, leading to a first pressure correction $\Delta p_B \approx 0.8$ kbar whereas for sample C, $\Delta p_C \approx 0.5$ kbar. The resistivity derivatives as a function of temperature can be used to extract the structural transition temperature T_s, as demonstrated in Fig. SM1B and C. These results suggests that T_s of sample B at 3.5 kbar is similar to that of sample A at 4.9 kbar, which would correspond to a pressure offset of $\Delta p_B \gtrsim 1.4$ kbar. Furthermore, at 4.7 kbar (sample B) no transition can be resolved, suggesting $\Delta p_B \gtrsim 1.2$. For sample C, we cannot deduce a definitive pressure correction as no transition could be resolved, which are likely to occur at higher temperatures. Nevertheless, we can infer an upper limit $\Delta p_C < 0.8$ kbar.

Another method to compare the pressure evolution of samples A-C is to compare their residual resistivity ratios (RRR) between the room temperature resistivity and that at the onset of superconductivity. Determining the pressure offset from RRR has the added benefit, in comparison to the absolute resistivity (Fig. SM1A) that it is insensitive to uncertainties in the contact layout. RRR of sample A increases substantially as the nematic phase is suppressed, and almost doubles between zero pressure and p_c, as shown in Fig. SM2. The best match of the RRR values between sample A and those of samples B and C, is achieved if one assumes pressure offsets of $\Delta p_B \approx 0.9$ kbar and $\Delta p_C \approx 0.4$ kbar, respectively.

Next, we directly address the position of each sample in the nematic phase diagram. The disappearance of a low-frequency quantum oscillation frequency has been previously interpreted as a Lifshitz transition which occurs at the nematic quantum phase transition [1, 3]. A

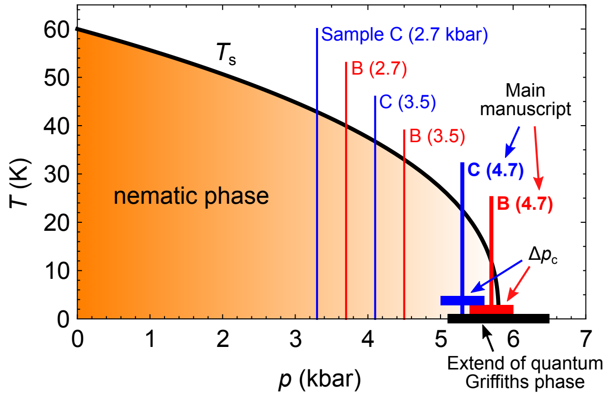

FIG. SM4. Pressure-temperature phase diagram of $FeSe_{0.89}S_{0.11}$. The position of samples B and C within the nematic phase based on sample A is indicated as a function of the reported pressure. These variations for high quality single crystals from the same batch occur due to the small variation in Se/S ratio. The horizontal bars indicate the pressure uncertainty due to the pressure correction for sample B and C (red, blue), and the experimental pressure range of the quantum Griffiths phase, as discussed in the main manuscript.

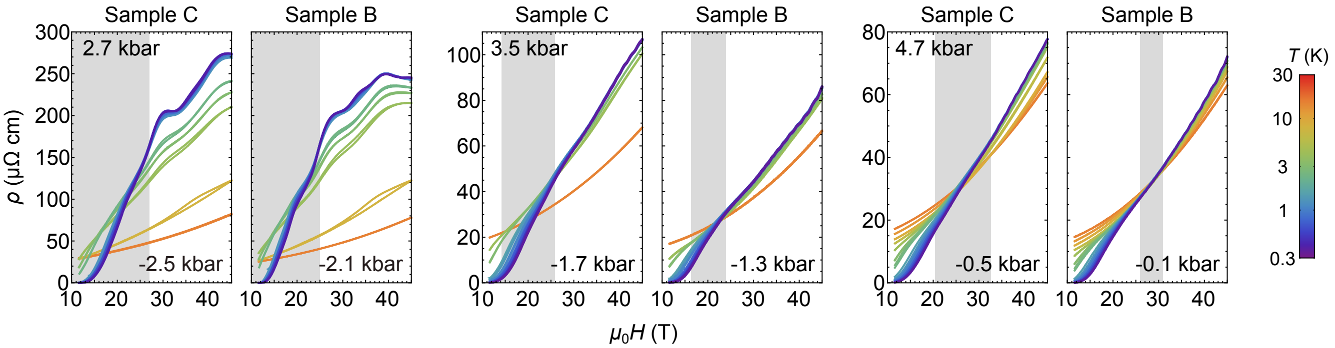

FIG. SM5. Pressure evolution of the magnetoresistivity crossing in samples B and C for temperatures $T \lesssim 15\,\mathrm{K}$. The shaded area marks the field range over which crossings can be observed. Pressures given in the top-left corner indicate the measured value, whereas the pressure value given in the bottom-right corner indicate the distance to the nematic quantum phase transition.

low-frequency quantum oscillation is clearly present for sample C, but absent in sample B at 4.7 kbar, as shown in the first derivative of the magnetoresistivity in Fig. SM3. Hence, we can infer that sample C is still within the nematic phase at 4.7 kbar, whilst sample B is at the nematic quantum phase transition (within experimental pressure resolution).

Based on all these different approaches, our best estimates for the pressure offsets in samples B and C, which we attribute to small variations in the sulfur content, are as follows:

$$\Delta p_{\mathrm{B}} \approx (1.0 \pm 0.3)\,\mathrm{kbar} \quad (1)$$

$$\Delta p_{\mathrm{C}} \approx (0.6 \pm 0.3)\,\mathrm{kbar} \quad (2)$$

These pressure offsets mark the position of samples B and C under pressure within the nematic phase, having sample B at $p = 4.7\,\mathrm{kbar}$ basically located at the nematic quantum phase transition, (within experimental uncertainty) as shown in Fig. SM4.

Evolution of the magnetoresistivity crossing with pressure in different samples

Fig. SM5 shows the magnetoresistivity data for samples B and C as a function of temperature and pressure up to $p = 4.7\,\mathrm{kbar}$ using common temperature range for all pressures $0.3\,\mathrm{K} \lesssim T \lesssim 15\,\mathrm{K}$ for a easier comparison. The order of the panels in Fig. SM5 corresponds to their relative position within the nematic phase as determined from Fig. SM4. With increasing pressure, or equivalently with *decreasing* distance to the nematic quantum phase transition, the field range of magnetoresistivity crossings becomes narrower, and it moves to higher fields (shaded area in Fig. SM5). The crossing collapses to a single point in sample B at 4.7 kbar which is the data set that is extensively discussed in the main paper.

Superconductivity

Figure SM6A shows the temperature and pressure dependence of the critical fields H_{c2}^{off}, H_{c2}^{on} and H_{c2}^{G} describing the offset, onset and additional shoulder of the normal-to-superconductor transitions of sample A (see main paper for their definitions). Also shown are the low-order polynomial fits used to extrapolate the zero-temperature values $H_{c2}^{\mathrm{off}}(0)$, $H_{c2}^{\mathrm{on}}(0)$ and $H_{c2}^{\mathrm{G}}(0)$. A linear polynomial has been used unless the data clearly displays a visible curvature. For a refined error estimate of $H_{c2}^{\mathrm{G}}(0)$, both linear and third order polynomials are shown as well. Importantly, the polynomial order used does not qualitatively change the main finding, i.e. a peak in $H_{c2}^{\mathrm{G}}(0)$ at the nematic quantum critical point, shown in Fig. SM6B and C.

Figure SM7 compares the evolution of the zero-field and of the zero-temperature superconducting transitions as a function of pressure across the nematic quantum phase transition. Panels A and B show that the transitions from the normal to the superconducting phase in zero field and finite temperatures are sharp for all pressures, which rules out effects from possible pressure inhomogeneities. The extracted evolution of T_c^{off} and T_c^{on} with pressure are shown in Panel C. When compared to the evolution of the zero-temperature limits of H_c^{off} and H_c^{on} (Panel D), this shows that the overall suppression of $T_c^{\mathrm{off/on}}$ and $H_{c2}^{\mathrm{off/on}}$ are similar. The marked difference is the emergence of the peak in H_{c2}^{G} which exists only in the low-temperature/high-field limit.

Normal state magnetoresistivity

We estimate the normal zero-field resistivity at low temperature for sample B at 4.7 kbar by extrapolating from the high-field magnetoresistivity data above the onset of superconductivity using a two-band model, as shown in Fig. SM8A. Assuming an electron- and a hole-

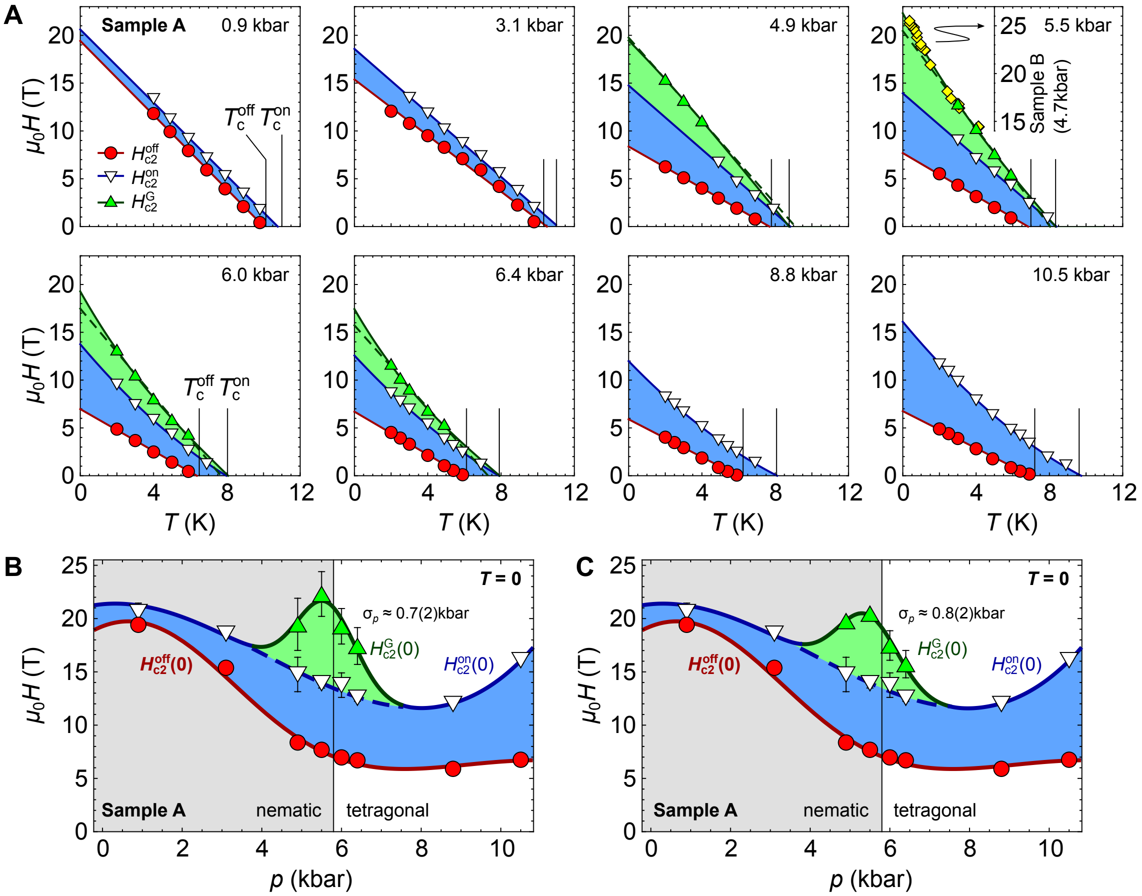

FIG. SM6. **(A)** Temperature and pressure dependence of the critical fields $H_{c2}^{\rm off}$, $H_{c2}^{\rm on}$ and $H_{c2}^{\rm G}$ of sample A. In the panel corresponding to $p = 5.5$ kbar, the onset field of sample B is included for reference (including a vertical offset of 4 T). Solid lines correspond to low-order polynomial fits (typically first order, maximum third order). The dashed lines represent first order fits for comparison. The thin vertical lines indicate $T_c^{\rm off}$ and $T_c^{\rm on}$ extracted from the cooling curves [1]. **(B,C)** Zero-temperature extrapolations $H_{c2}^{\rm off}$, $H_{c2}^{\rm on}$ and $H_{c2}^{\rm G}$ using best fits (B) or linear extrapolations (C) for $H_{c2}^{\rm G}$. The peak in $H_{c2}^{\rm G}$ occurs independently of the fitting function. Panel B shows the same data as the inset of Fig. 4(g) of the main paper.

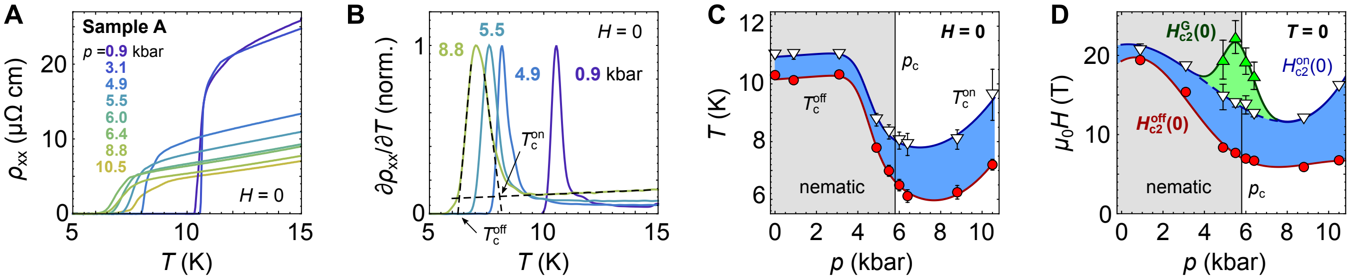

FIG. SM7. Evolution of the zero-field superconducting transition across the nematic quantum phase transition. **(A)** Cool-down resistivity curves across the superconducting transition and **(B)** the normalized derivatives thereof. The transition remains sharp and single-stepped across the nematic quantum phase transition, in contrast to the field-induced transition shown in Fig. 4 of the main paper. **(C)** Pressure dependence of the onset and offset temperatures $T_c^{\rm on}$ and $T_c^{\rm off}$ in zero field. **(D)** Pressure dependence of the onset and offset critical fields $H_{c2}^{\rm on}$, $H_{c2}^{\rm off}$ and $H_{c2}^{\rm G}$ extracted in the zero-temperature limit (identical to the inset of Fig. 4(g)) of the main paper.

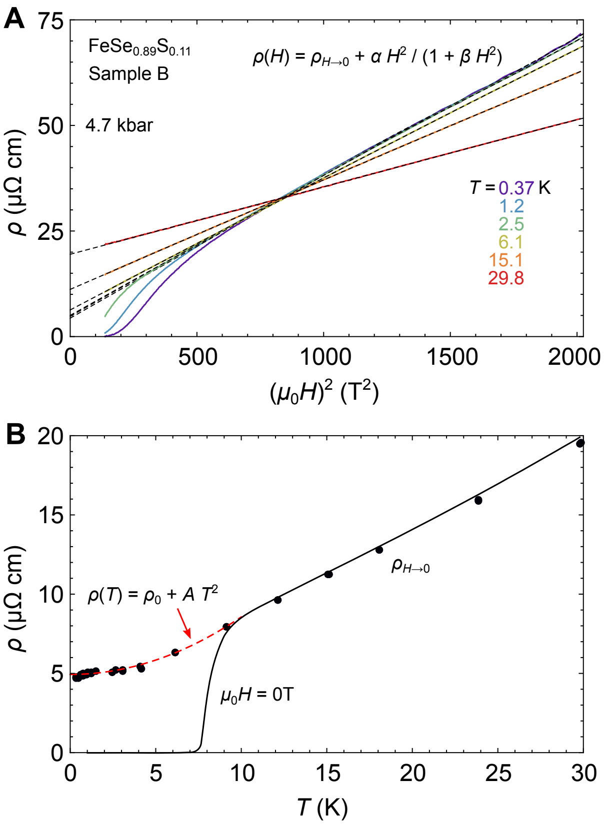

FIG. SM8. (**A**) A two-band model is used to describe the magnetoresistivity data above the onset of superconductivity. (**B**) The extrapolated zero-field resistivity, $\rho_{H\to0}$, are obtained from the fits in panel A (dots) and the zero-field resistivity data is shown by the solid line. The red dashed line is a fit to the Fermi liquid behavior, $\rho_0 + AT^2$ at low temperatures with $\rho_0 \approx 4.9\,\mu\Omega\,\mathrm{cm}$ and $A \approx 0.036\,\mu\Omega\,\mathrm{cm/K^2}$. Deviations below $T \approx 2\,\mathrm{K}$ are caused by the presence of quantum oscillations at high fields. Panel B is reproduced from Fig. 2(d) of the main paper for reference.

like band with charge carrier densities and mobilities n_e, n_h, μ_e, μ_h, respectively, the magnetoresistivity is given by

$$\rho(B) = \frac{(\mu_e n_e + \mu_h n_h) + \mu_e \mu_h (\mu_e n_h + n_e \mu_h) B^2}{e(\mu_e n_e + \mu_h n_h)^2 + e\mu_e^2 \mu_h^2 (n_e - n_h)^2 B^2} \tag{3}$$

where e is the electron charge. We can re-write the above expression as

$$\rho(B) = \frac{1}{e(\mu_h n_h + \mu_e n_e)} + \frac{\mu_e n_e \mu_h n_h (\mu_e + \mu_h)^2 B^2}{e(\mu_e n_e + \mu_h n_h)^3 + e\mu_e^2 \mu_h^2 (n_e - n_h)^2 (\mu_e n_e + \mu_h n_h) B^2} \tag{4}$$

from which we identify the zero-field limit $\rho_{H\to0} = (e(\mu_h n_h + \mu_e n_e))^{-1}$. Next, we substitute

$$\alpha = \mu_0^2 \frac{\mu_e n_e \mu_h n_h (\mu_e + \mu_h)^2}{e(\mu_e n_e + \mu_h n_h)^3} \tag{5}$$

$$\beta = \mu_0^2 \frac{\mu_e^2 \mu_h^2 (n_e - n_h)^2}{(\mu_e n_e + \mu_h n_h)^2} \tag{6}$$

and we assume a non-magnetic environment $B = \mu_0 H$ which allows us to write

$$\rho(H) = \rho_{H\to0} + \frac{\alpha H^2}{1 + \beta H^2}. \tag{7}$$

In this notation, α effectively measures the strength of the magnetoresistivity which depends on the charge carrier densities and their mobilities. Furthermore, β measures the deviations away from a compensated two-band system, i.e. if $n_e = n_h$ then $\beta = 0$. From previous ARPES, quantum oscillation and magnetoresistivity studies, it is well known that ambient pressure FeSe$_{0.89}$S$_{0.11}$ is a compensated four-band system, which is dominated by two large, nearly compensated bands [1, 3–5]. The above two-band model fit therefore provides a simplified description and we expect $\beta > 0$, effectively encapsulating the contributions from the two smaller bands.

From Fig. SM8A, we find a good description of the data with only minor deviations visible at temperatures below $T \lesssim 2\,\mathrm{K}$ and fields $\mu_0 H \gtrsim 35\,\mathrm{T}$ which we attribute to the appearance of quantum oscillations. The extracted temperature dependence of $\rho_{H\to0}(T)$ is shown in Fig. SM8B, together with the zero-field cool down resistivity. For temperatures $T \lesssim 10\,\mathrm{K}$ the extracted zero-field resistivity is consistent with Fermi liquid behavior $\rho \sim T^2$, in good agreement with the previously reported low-temperature dependence of sample A [1]. Overall, this confirms that the normal state resistivity is consistent with predictions for a multi-band Fermi liquid.

Temperature dependent scaling of the magnetoresistivity

From Equation 1 in the main manuscript, we can extract the exponent $z\nu$ from the slope of a log-log plot of the derivative of the magnetoresistivity,

$$\log\left[\partial\rho/\partial(\mu_0 H)\right]|_{H=H^\star} = -1/z\nu \log(T) + \mathrm{const}, \tag{8}$$

which is shown in Fig. 3(a) in the main manuscript for temperatures above the onset of quantum oscillations ($\sim 2\,\mathrm{K}$). Consistent results are obtained using a second method in which the scaling relation, Eq. 1, is applied to all curves in fields $H > H_{c2}^{\mathrm{on}}$ over small temperature intervals, which allows us to extract $z\nu$ per interval, as discussed below.

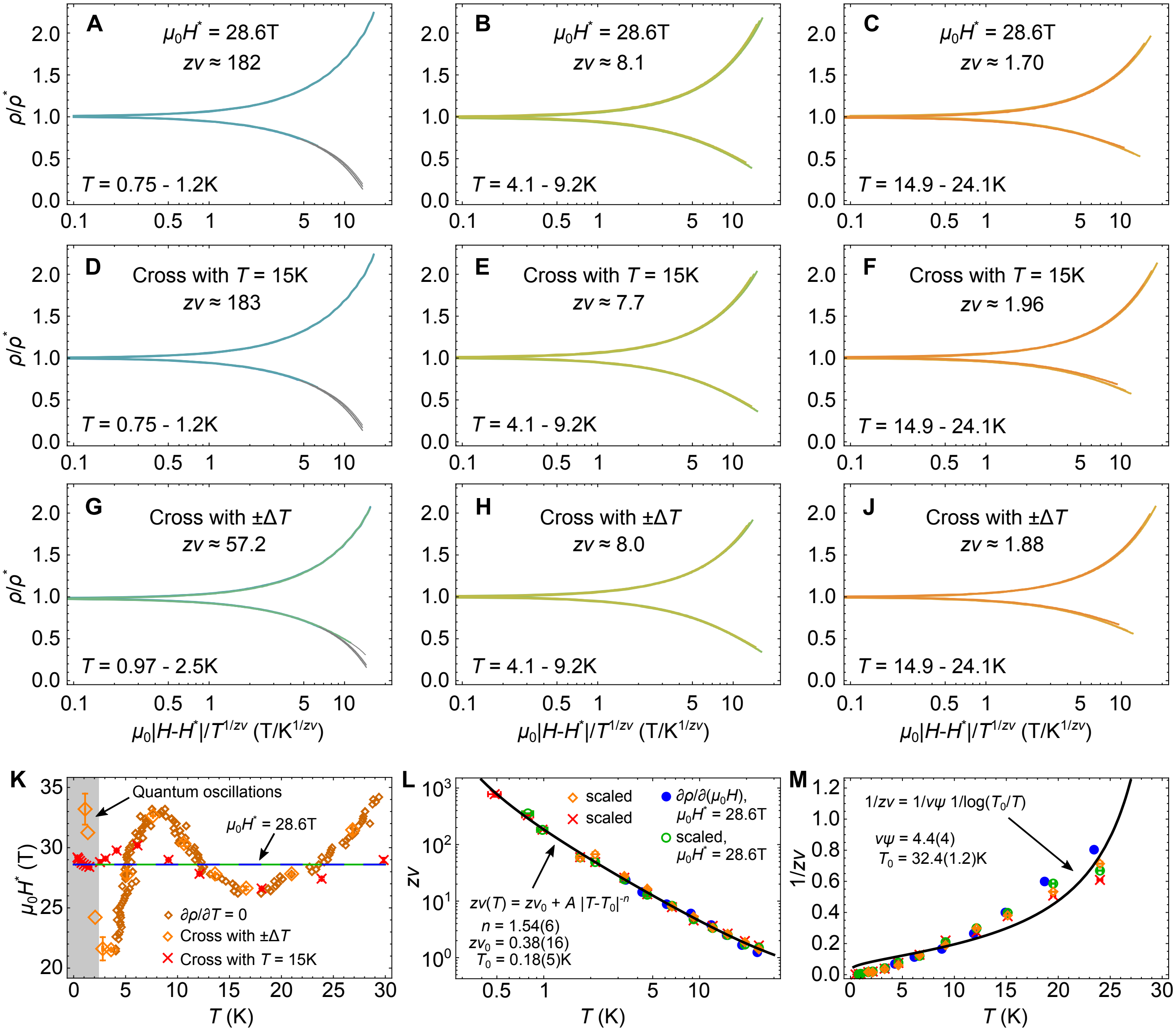

FIG. SM9. **(A)-(J)** Representative examples of the scaling analysis over finite temperature ranges. The spread of the scaled magnetoresistivity data is minimized by varying $z\nu$ as the only parameter. The magnetoresistivity crossing point was either fixed in field $\mu_0H^\star = 28.6\,\mathrm{T}$ (Panels A-C), obtained from the intersection with the $T = 15\,\mathrm{K}$ dataset (Panels D-F), or from the intersection with neighbouring temperature runs (Panels G-J). **(K)** The temperature dependence of the magnetoresistivity crossing field obtained by the same methods. **(L)** Temperature dependence of $z\nu$. The solid line shows a fit to a generalized power-law form, with the obtained fitting parameters given. **(M)** Same data as in Panel L. The solid line shows a fit assuming activated behavior. Symbols in panels L and M correspond to the same crossing method as indicated in panel K. Errors in panels L and M represent a 1σ confidence interval.

Fig. SM9 shows in detail the scaling analysis of the magnetoresistivity crossing in sample B, which is summarized in the main text. First, the magnetoresistivity over any given temperature range is being rescaled using a manually estimated value for the $z\nu$ parameter (panels A-H). Subsequently, $z\nu$ is obtained by fitting the upper and lower branches independently using a high order polynomial (consistently 7th order, excluding field data below the onset of superconductivity), and then by minimizing the total residual to a global minimum by varying $z\nu$ as the only free parameter. The differences between the panels concern the method how the magnetoresistivity crossing was determined. In Panels A-C, the crossing was set to a constant field $\mu_0H^\star = 28.6\,\mathrm{T}$ and $\rho^\star = 32.1\,\mu\Omega\,\mathrm{cm}$, consistent with the derivative analysis presented in the main paper (shown as a dashed line in

Panel J). In Panels D-F, the crossing field $H^{\star}(T)$ is defined as the intersection of the magnetoresistivity at temperature T with the magnetoresistivity at $T \approx 15\,\mathrm{K}$. The advantage of this procedure is that it can be carried out for all temperatures reliably, and the fields obtained are shown in Panel K (crosses). Finally, in Panels G-J, the crossing is defined between two adjacent temperatures measured (shown as large diamonds in Panel K). Equivalently, the crossings are given by tracing the trajectory $\partial\rho/\partial T = 0$ as a function of T and H (shown as small diamonds in Panel K). This method becomes unreliable at lowest temperatures for two reasons: firstly quantum oscillations are not governed by the scaling relation and thus, the true crossing can be masked; secondly, $z\nu$ becomes very large at low-temperatures so that the temperature dependence term in the scaling relation $T^{-1/z\nu}$ becomes effectively constant, and the crossing is smeared by noise.

While the various extraction methods yield different crossing fields in Fig. SM9K, the extracted values for $z\nu$ are only marginally affected (Fig. SM9L). Importantly, the divergence of $z\nu$ towards low temperatures is not influenced by the chosen method. Next, to test for deviations from a pure power-law form at highest or lowest temperatures, we employ a generalized power-law form given by:

$$z\nu(T) = z\nu_0 + A|T - T_0|^{-n} \tag{9}$$

where $z\nu_0$ describes the high-temperature (i.e. the non-Griffiths) part, and T_0 describes the temperature at which $z\nu$ diverges. Within experimental uncertainty (errors are given as a 1σ confidence interval), $z\nu$ is found to diverge close to zero temperature ($T_0 \approx 0.18(5)\,\mathrm{K}$) (Fig. SM9L). However, the true uncertainty in T_0 is presumably larger than the statistical value obtained from the fit in Panel L. This is because the temperature uncertainty for the $T \approx 370\,\mathrm{mK}$ dataset could be in excess of $40\,\mathrm{mK}$, as the sample inside the cell is away from the outside thermometer. Finally, $z\nu_0$ is consistent with mean-field behavior in the presence of long-range interactions for which $z\nu_0 = 0.5$ [6]. Fig. SM9M shows the best fit of $z\nu(T)$ assuming activated behavior [7], which clearly fails to describe the data, in contrast to the good description assuming power-law behavior (Fig. SM9L).

Extend of the quantum Griffiths phase

Figure SM10 shows the range over which the scaling relation, Eq. 1 of the main manuscript, applies to describe the magnetoresistivity of sample B at a pressure of $p = 4.7\,\mathrm{kbar}$. Evidently, the scaling relation applies to nearly the entire H-T phase space studied. The upper limit marks a crossover from the quantum critical region at low temperatures to the classical region where the scaling form breaks down. The lower limit coincides with the onset of superconductivity, demonstrating that the scaling relation describes the normal (non-superconducting) state.

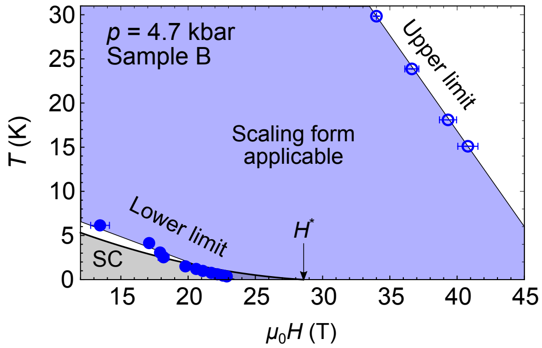

FIG. SM10. Limits of the applicability of the scaling relation, Eq. 1 of the main manuscript, to the magnetoresistivity of sample B at a pressure of $p = 4.7\,\mathrm{kbar}$. At the upper and lower limits, deviations of the scaling form occur. The lower limit coincides with the onset of superconductivity (SC).

Parallel resistor network of mixed phases

In the highest measured magnetic field of $\mu_0 H = 45\,\mathrm{T}$, the resistivity $\rho(T)$ above $10\,\mathrm{K}$ displays an approximately exponential increase, characteristic for insulating-like be-

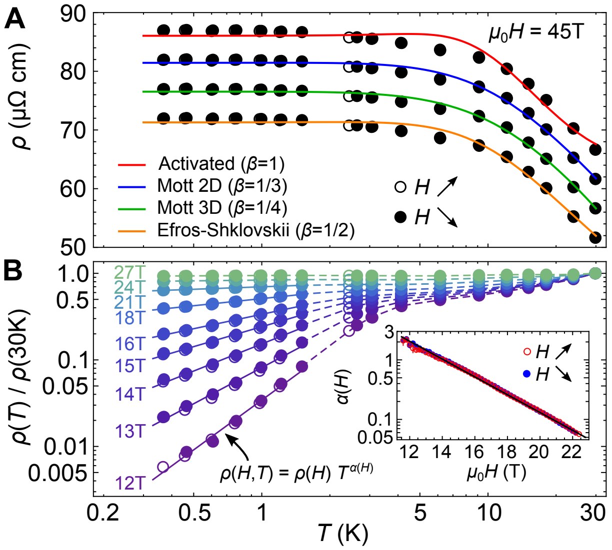

FIG. SM11. High-field and low-field resistivity as function of temperature. (A) In high fields, the data can be described by a phenomenological parallel network of metallic and insulating behavior. Experimental data points and fits are incrementally offset by $+5\,\mu\Omega\,\mathrm{cm}$ for clarity. (B) At low-fields, the resistivity below $2\,\mathrm{K}$ follows a power-law form which implies $\rho \to 0$ for $t \to 0$, and $T_c = 0$. The inset shows the nearly exponential field-dependence of the power-law exponent.

havior, as shown in Fig. SM11A. At lower temperatures, a cross-over occurs around 5 K, and $\rho(T)$ saturates below 2 K which is the regime where quantum oscillations become the strongest (Fig. 2 in the main paper). This behavior can be described using a phenomenological model consisting of a parallel network of insulating and metallic conductivities, σ_{ins} and σ_{m}, respectively, given by

$$\sigma_{\mathrm{m}}^{-1}(T) = \rho_0(45\,\mathrm{T}) + AT^2 \tag{10}$$

$$\sigma_{\mathrm{ins}}^{-1}(T) = s\exp((U/k_{\mathrm{B}}T)^{\beta}) \tag{11}$$

$$\rho(T, 45\,\mathrm{T}) = (\sigma_{\mathrm{m}} + \sigma_{\mathrm{ins}})^{-1}\,. \tag{12}$$

Here, we assume Fermi liquid-like behavior for the metallic part of the conductivity with $A = 0.036\,\mu\Omega\,\mathrm{cm/K}^2$, as obtained for the extrapolated zero-field resistivity shown in Fig. SM8, and which is consistent with previous observations [1]. For the insulating contribution to the total conductivity, U is a characteristic energy scale, and s describes the high temperature conductivity which is lost for $T \to 0$ (k_{B} is the Boltzmann constant). The exponent β depends on the appropriate conduction process and the dimensionality: for activated behavior, $\beta = 1$, whereas variable-range Mott-hoping gives $\beta = 1/(1+d)$ where d is the spatial dimension [8–10]. Including the effects of a Coulomb gap, the Elfros-Shklovskii variable-range hopping leads to $\beta = 1/2$ for all dimensions [11, 12]. Consequently, this phenomenological model gives $\rho(T \to 0, H) = \rho_0(H)$ which ensures a finite metallic conductivity at low temperatures, whereas $\rho(T)$ decays as $\exp(-U/T)$ for higher temperatures, ensuring insulating-like behavior there, as observed in Fig. SM11A. Treating ρ_0, U and s as fitting parameters, we compare the fits of this model for different fixed β to the experimental data in Fig. SM11A. We find that for all values of β, the model broadly captures the temperature dependence of the resistivity observed. We therefore cannot infer which conduction process is the most fitting, but it appears that activated behavior ($\beta = 1$) provides the poorest description. Thus, we speculate that a partial localization might take place in high magnetic fields, reminiscent of the high-field insulating phases of systems where quantum Griffiths phases were observed [7, 13–20].

---

[*] p.reiss@fkf.mpg.de; Current address: Max-Planck Institute for Solid State Research, Stuttgart, Germany

[†] amalia.coldea@physics.ox.ac.uk

[1] Pascal Reiss, David E. Graf, Amir A. Haghighirad, William Knafo, Loïc Drigo, Matthew Bristow, Andrew J Schofield, and Amalia I. Coldea, "Quenched nematic criticality and two superconducting domes in an iron-based superconductor," Nature Physics **16**, 89–94 (2020).

[2] A. E. Böhmer, V. Taufour, W. E. Straszheim, Thomas Wolf, and P. C. Canfield, "Variation of transition temperatures and residual resistivity ratio in vapor-grown FeSe," Physical Review B **94**, 024526 (2016).

[3] Amalia I. Coldea, Samuel F. Blake, Shigeru Kasahara, Amir A. Haghighirad, Matthew D. Watson, William Knafo, Eun Sang Choi, Alix McCollam, Pascal Reiss, Takuya Yamashita, Mara Bruma, Susannah C. Speller, Yuji Matsuda, Thomas Wolf, Takasada Shibauchi, and Andrew John Schofield, "Evolution of the low-temperature Fermi surface of superconducting $\mathrm{FeSe}_{1-x}\mathrm{S}_x$ across a nematic phase transition," npj Quantum Materials **4**, 2 (2019).

[4] Matthew D Watson, Timur K Kim, Amir A Haghighirad, Samuel F Blake, N R Davies, M Hoesch, Thomas Wolf, and Amalia I Coldea, "Suppression of orbital ordering by chemical pressure in $\mathrm{FeSe}_{1-x}\mathrm{S}_x$," Physical Review B **92** (2015), 10.1103/PhysRevB.92.121108.

[5] M. Bristow, P. Reiss, A. A. Haghighirad, Z. Zajicek, S. J. Singh, T. Wolf, D. Graf, W. Knafo, A. McCollam, and A. I. Coldea, "Anomalous high-magnetic field electronic state of the nematic superconductors $\mathrm{FeSe}_{1-x}\mathrm{S}_x$," Phys. Rev. Research **2**, 013309 (2020).

[6] Sebastian Fey, Sebastian C. Kapfer, and Kai Phillip Schmidt, "Quantum Criticality of Two-Dimensional Quantum Magnets with Long-Range Interactions," Physical Review Letters **122**, 017203 (2019), arXiv:1802.06684.

[7] Nicholas A. Lewellyn, Ilana M. Percher, Jj Nelson, Javier Garcia-Barriocanal, Irina Volotsenko, Aviad Frydman, Thomas Vojta, and Allen M. Goldman, "Infinite-randomness fixed point of the quantum superconductor-metal transitions in amorphous thin films," Physical Review B **99**, 054515 (2019).

[8] N. F. Mott, "Conduction in non-crystalline systems," Philosophical Magazine **17**, 1259–1268 (1968).

[9] N. F. Mott, "Conduction in non-crystalline materials," Philosophical Magazine **19**, 835–852 (1969).

[10] N. F. Mott, "Metal-insulator transitions," Pure and Applied Chemistry **52**, 65–72 (1980).

[11] A. L. Efros and B. I. Shklovskii, "Coulomb gap and low temperature conductivity of disordered systems," Journal of Physics C: Solid State Physics **8**, L49–L51 (1975).

[12] A. L. Efros, "Coulomb gap in disordered systems," Journal of Physics C: Solid State Physics **9**, 2021–2030 (1976).

[13] Matthew P. A. Fisher, "Quantum phase transitions in disordered two-dimensional superconductors," Physical Review Letters **65**, 923–926 (1990).

[14] G. T. Seidler, T. F. Rosenbaum, and B. W. Veal, "Two-dimensional superconductor-insulator transition in bulk single-crystal $\mathrm{YBa}_2\mathrm{Cu}_3\mathrm{O}_{6.38}$," Physical Review B **45**, 10162–10164 (1992).

[15] R. Schneider, A. G. Zaitsev, D. Fuchs, and H. v. Löhneysen, "Superconductor-Insulator Quantum Phase Transition in Disordered FeSe Thin Films," Physical Review Letters **108**, 257003 (2012).

[16] Xiaoyan Shi, Ping V. Lin, T. Sasagawa, V. Dobrosavljević, and Dragana Popović, "Two-stage magnetic-field-tuned superconductor-insulator transition in underdoped $\mathrm{La}_{2-x}\mathrm{Sr}_x\mathrm{CuO}_4$," Nature Physics **10**, 437–443 (2014).

[17] Ying Xing, H.-M. Zhang, H.-L. Fu, Haiwen Liu, Yi Sun, J.-P. Peng, F. Wang, Xi Lin, X.-C. Ma, Q.-K. Xue, Jian Wang, and X. C. Xie, "Quantum Griffiths singularity of superconductor-metal transition in Ga thin films," Science **350**, 542–545 (2015).

[18] Yu Saito, Tsutomu Nojima, and Yoshihiro Iwasa, "Quantum phase transitions in highly crystalline two-dimensional superconductors," Nature Communications

9, 778 (2018).

[19] Yi Liu, Ziqiao Wang, Pujia Shan, Yue Tang, Chaofei Liu, Cheng Chen, Ying Xing, Qingyan Wang, Haiwen Liu, Xi Lin, X. C. Xie, and Jian Wang, "Anomalous quantum Griffiths singularity in ultrathin crystalline lead films," Nature Communications **10**, 3633 (2019).

[20] Yen Hsiang Lin, J. Nelson, and A. M. Goldman, "Superconductivity of very thin films: The superconductor-insulator transition," Physica C: Superconductivity and its Applications **514**, 130–141 (2015).